Acta Pharmaceutica Sinica B 2022;12(3):1416–1431

Chinese Pharmaceutical Association
Institute of Materia Medica, Chinese Academy of Medical Sciences

Acta Pharmaceutica Sinica B

www.elsevier.com/locate/apsb
www.sciencedirect.com

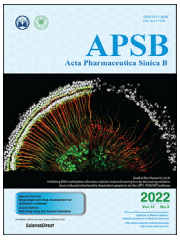

ORIGINAL ARTICLE

Co-delivery of photosensitizer and diclofenac through sequentially responsive bilirubin nanocarriers for combating hypoxic tumors

Yang Zhou[a], Fan Tong[a], Weilong Gu[a], Siqin He[a], Xiaotong Yang[a], Jiamei Li[a], Yue-Dong Gao[b,c,*], Huile Gao[a,*]

[a]*Key Laboratory of Drug-Targeting and Drug Delivery System of the Education Ministry, Sichuan Engineering Laboratory for Plant-Sourced Drug and Sichuan Research Center for Drug Precision Industrial Technology, West China School of Pharmacy, Sichuan University, Chengdu 610064, China*
[b]*Core Technology Facility of Kunming Institute of Zoology, Chinese Academy of Sciences, Kunming 650223, China*
[c]*Chinese Academy of Sciences Territorial Core Facility of Kunming Biological Diversity Regional Center, Kunming 650223, China*

Received 18 August 2021; received in revised form 24 October 2021; accepted 17 November 2021

KEY WORDS

Bilirubin nanoparticles;
ROS-responsive drug release;
Charge reversal;
Photodynamic therapy;
Hypoxia;
Diclofenac;
LDHA inhibition;
HIF-1α inhibition

Abstract Considering that photodynamic therapy (PDT)-induced oxygen consumption and microvascular damage could exacerbate hypoxia to drive more glycolysis and angiogenesis, a novel approach to potentiate PDT and overcome the resistances of hypoxia is avidly needed. Herein, morpholine-modified PEGylated bilirubin was proposed to co-deliver chlorin e6, a photosensitizer, and diclofenac (Dc). In acidic milieu, the presence of morpholine could enable the nanocarriers to selectively accumulate in tumor cells, while PDT-generated reactive oxidative species (ROS) resulted in the collapse of bilirubin nanoparticles and rapid release of Dc. Combining with Dc showed a higher rate of apoptosis over PDT alone and simultaneously triggered a domino effect, including blocking the activity and expression of lactate dehydrogenase A (LDHA), interfering with lactate secretion, suppressing the activation of various angiogenic factors and thus obviating hypoxia-induced resistance-glycolysis and angiogenesis. In addition, inhibition of hypoxia-inducible factor-1α (HIF-1α) by Dc alleviated hypoxia-induced resistance. This study

*Corresponding authors. Tel./fax: +86 187 80288069 (Huile Gao); +86 136 48811007 (Yue-Dong Gao).
E-mail addresses: gaoyd@mail.kiz.ac.cn (Yue-Dong Gao), gaohuile@scu.edu.cn (Huile Gao).

Peer review under responsibility of Chinese Pharmaceutical Association and Institute of Materia Medica, Chinese Academy of Medical Sciences.

https://doi.org/10.1016/j.apsb.2021.12.001

offered a sequentially responsive platform to achieve sufficient tumor enrichment, on-demand drug release and superior anti-tumor outcomes *in vitro* and *in vivo*.

1. Introduction

Photodynamic therapy (PDT) has emerged as an appealing and potent treatment modality against solid tumors, wherein upon exposure to irradiation, photosensitizer could generate highly toxic reactive oxidative species (ROS) to eradicate malignant cells directly through apoptosis and indirectly by induction of vascular shutdown and recruitment of immune mediators[1]. However, most PDT agents consume oxygen (O_2) to produce ROS, coupled with vascular shutdown, which can aggravate the intrinsic hypoxia within tumors[2]. Through induction and stabilization of hypoxia-inducible factor-1α (HIF-1α), it would result in two potential resistance mechanisms: one is metabolic reprogramming from oxidative phosphorylation (OXPHOS) to glycolysis, including the upregulation of hexokinase 2 (HK2), lactate dehydrogenase A (LDHA) and monocarboxylic acid transporter-4 (MCT-4), to reduce their reliance on O_2, while the other is enhanced secretion of various pro-angiogenic factors such as vascular endothelial growth factor (VEGF) and angiopoietin (ANGPT), to trigger angiogenesis and increase O_2 supply[3−5]. Worse yet, increased glycolysis will engender copious amount of lactate, and lactate is shuttled between glycolytic cancer cells and angiogenic endothelial cells by MCT[6], which stimulates VEGF-α/VEGFR2 production through the HIF-dependent pathway[7,8], activates nuclear factor-kappa B (NF-κB)-mediated proangiogenic interleukin-8 (IL-8) signaling[9] as well as binds to and stabilizes N-MYC downstream-regulated protein (NDRG3)[10] to fuel angiogenesis, tumor regrowth and metastasis during prolonged hypoxia. For this reason, it is highly feasible to disrupt PDT-triggered glycolysis and angiogenesis, so as to potentiate the efficacy of PDT against hypoxic tumors.

In the context of lactate metabolism, LDHA preferentially converts pyruvate to lactate, accompanied by NADH oxidation to NAD^+, while another subtype LDHB could reoxidize lactate to pyruvate to drive OXPHOS. MCT1 or MCT4 is responsible for lactate transport between oxidative cells and glycolytic cells[11]. Among these, LDHA, a key enzyme in glycolysis, could produce lactate and its expression, primarily regulated by several important transcription factors, including c-MYC and HIF-1α[12−14]. Following the LDHA inhibition by FX11 or shRNA, it led to ROS production and decreased energy levels, resulting in apoptotic cell death. Glycolysis-dependent cell lines were more susceptible to LDHA blockade, relative to oxidative cells[15,16]. Besides, LDHA expression was positively correlated with the activation of VEGF/VEGFR2 signaling pathway, and regulating angiogenesis by LDHA is mainly dependent on the production of lactate[12,17]. Based on these findings, targeting LDHA could achieve its full potential in modulating both glycolysis and angiogenesis through lactate reduction, to augment the lethality of ROS to tumor in PDT. Diclofenac (Dc), one of non-steroidal anti-inflammatory drugs (NSAID), was found to significantly diminish c-MYC expression, and reduce LDHA and MCT1 gene expression with a decrease in lactate secretion[18], while other research showed decreased LDHA gene expression[19] or activity[20] in glioma cells. In addition, molecular docking revealed Dc could prominently interact with LDHA protein[21]. Compared with conventional inhibitor, like FX-11 and galloflavin, or LDHA siRNA, Dc was a relatively more affordable and safer alternative for combination therapy.

We thus hypothesized that the combined application of LDHA inhibitor Dc and photosensitizer chlorin e6 (Ce6) could provoke more ROS-potentiated apoptosis, while overcoming PDT-induced glycolysis and angiogenesis. However, for co-delivery of Dc and Ce6, obstacles such as hydrophobicity, poor pharmacokinetics behavior and insufficient tumor accumulation limit drugs' access to malignant cells, subsequently impeding the application of free drugs *in vivo*[22]. Furthermore, systemic administration of high-dose Ce6 and Dc could solve this, but induce a series of off-target effects and, for example, more ROS production by PDT causes more harm to the peripheral tissues around the tumor[23,24] and overdosing Dc triggers myocardial infarction, urinary system injury or liver dysfunction[25−27]. In view of this, the drug nanocarrier comes under the spotlight to address the aforementioned problems[28−30], as it features the following superiority: encapsulating hydrophobic drugs, accumulating in tumor tissues through the enhanced permeability and retention (EPR) effect, and on-demand drug release in respond to either external or internal signals.

Toward this end, our "proof-of-concept" strategy was built on an ideal platform —morpholine-modified bilirubin nanoparticles to co-deliver hydrophobic Ce6 and Dc (Ce6&Dc@MBNP) for combinatory phototherapy of 4T1 breast cancers (Fig. 1)[31,32]. Of note, much less is known about the effects of Dc on LDHA activity, protein expression and related upstream pathway in 4T1 cells. In this regard, its effect was systemically studied in 4T1 cells *in vitro*. Dc treatment inhibited LDHA through interfering with activity and decreasing its expression, which correlated with the obtained result that Dc downregulated its upstream proteins including HIF-1α[33] and c-MYC[18], while PDT induced slightly increased LDHA expression. We also evaluated the effects of Dc on B16F10, MCF-7 and HUVEC. Dc were verified to be more sensitive to glycolytic malignant cells, in consistent with recent literature[34]. Moreover, morpholine-decorated nanocarriers, which in blood circulation stayed neutral but became positively charged in acidic tumor microenvironment (TME), could achieve enhanced accumulation and endocytosis[35,36] by tumor cells. The hydrophobic core of nanocarriers could ensure excellent co-delivery of Dc and Ce6 simultaneously into cancer cells and prevent burst drug leakage, mainly through the $\pi-\pi$ stacking and hydrophobic interactions. Exposed to 650 nm near-infrared (NIR) laser irradiation, abundant ROS generation by Ce6 could disrupt bilirubin particles and concurrently achieve on-demand Dc release by hydrophobic-to-hydrophilic switch[37−39]. Apart from more tumor apoptosis induction, *in vivo* mechanism assay indicated the released Dc, like dominoes, downregulated LDHA, subdued

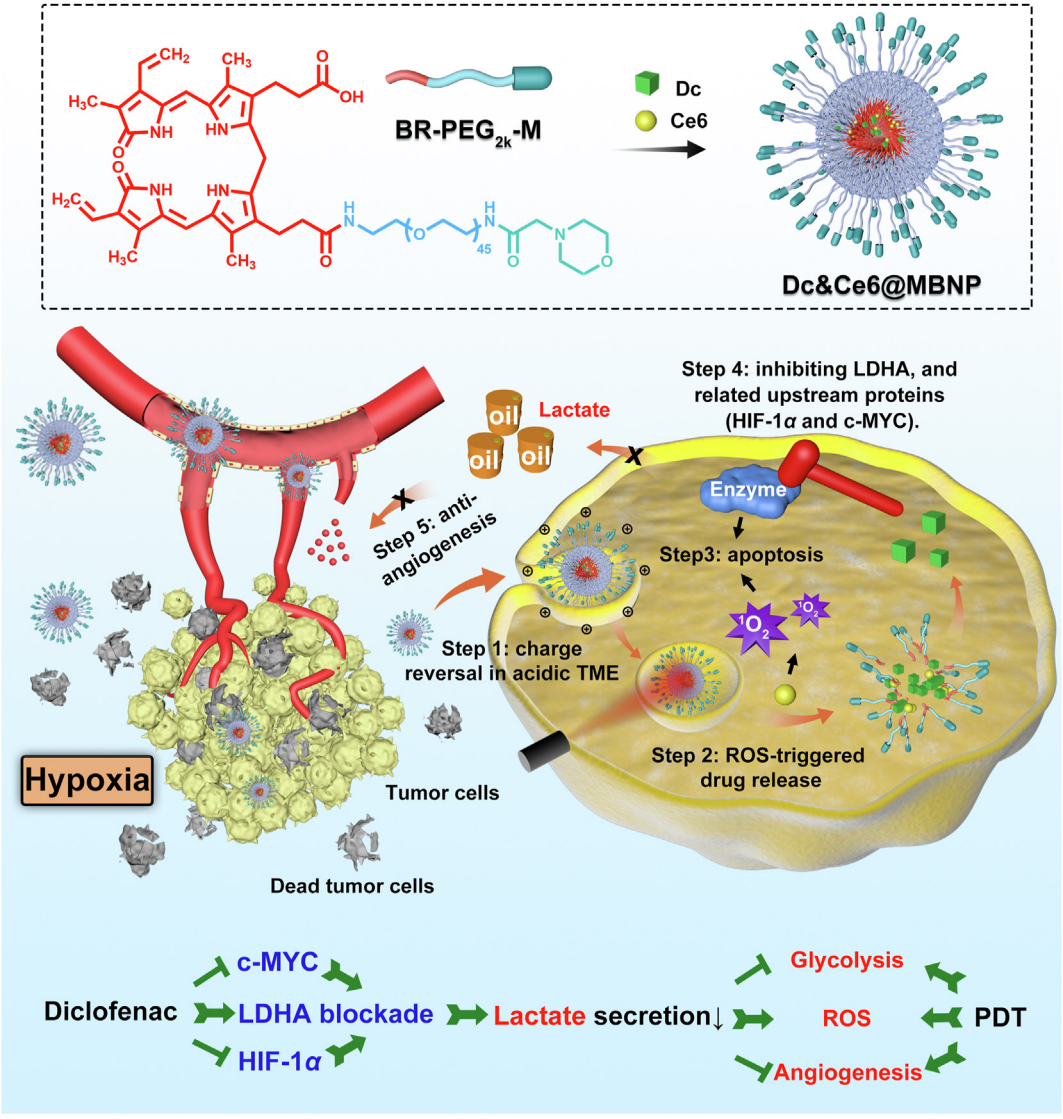

Figure 1 Schematic illustration of the composition of Dc&Ce6@MBNP and its synergistic anti-cancer mechanism.

lactate production and reduced VEGF, ANGPT and CD31 expression[40], thus interfering with PDT-triggered glycolysis and angiogenesis. In addition, inhibition of HIF-1α pathway by Dc also facilitated the efficacy of PDT. This simple and multifunctional nanocarrier might provide a compelling paradigm for phototherapy of breast cancers by inhibiting glycolysis, angiogenesis and the hypoxia pathway.

2. Materials and methods

2.1. *Materials*

Chlorin e6 was purchased from J&K Scientific Ltd. (Beijing, China). Diclofenac, morpholin-4-yl-acetic acid hydrochloride, 1-(3-dimethylaminopropyl)-3 ethylcarbodiimide hydrochloride (EDC), 4-dimethylaminopyridine (DMAP) and trimethylamine (TEA) were purchased from Aladdin (Shanghai, China). Bilirubin and *N,N′*-diisopropylcarbodiimide (DIC) were purchased from Tokyo Chemical Industry Co., Ltd. (Tokyo, Japan). mPEG$_{2k}$-NH$_2$ and Fmoc-NH-PEG$_{2k}$-NH$_2$ were purchased from Ponsure Biotechnology (Shanghai, China). Cou-6 was obtained from Sigma−Aldrich (USA). DiD and DCFH-DA were obtained from Meilunbio (Dalian, China). The annexin V-fluoresceine isothiocyanate (FITC) apoptosis detection kit and calcium-AM were obtained from Yeason (Shanghai, China). Lactate detection kit and lactate dehydrogenase assay kit were obtained from Nanjing Jiancheng Bioengineering Institute (Naijing, China). Anti-HIF-1α antibody, Cy3 goat anti-rabbit IgG (H + L) and Alexa fluor 647 goat anti-rabbit IgG (H + L) secondary antibody were purchased from Abcam (Hongkong, China). Anti-LDHA and anti-CD31 antibody were purchased from Servicebio Company (Wuhan, China). Anti-LDHB and anti-c-MYC antibody were purchased from Proteintech (Wuhan, China). Anti-VEGFα and anti-angiopoietin-2 antibody were purchased from Abclonal Company (Wuhan, China).

2.2. *Cell lines and animals*

Murine 4T1 breast cancer cells, HUVEC, MCF-7 and B16F10 were obtained from Chinese Academy of Sciences Cells Bank

(Shanghai, China). Complete RPMI-1640 or DMEM cell culture medium (containing 10% of fetal bovine serum, 100 U/mL of penicillin G, and 100 U/mL of streptomycin sulfate) was used to culture cells. Cells were maintained in incubator under a condition of 37 °C and 5% CO_2.

Female BALB/c mice (5−6 weeks, 18−22 g) were purchased from Ensiweier Biotechnology Co., Ltd. (Wuhan, China). All animal experiments were performed under the guidelines, evaluated and approved by the Ethics Committee of Sichuan University.

2.3. Synthesis of PEGylated bilirubin and morpholine-decorated PEGylated bilirubin

According to the literature[41], the synthesis method with minor modifications was as follows. Bilirubin (0.1 mmol) and EDC (0.15 mmol) were dissolved in 2 mL of dimethyl sulfoxide (DMSO), and stirred at room temperature for 10 min. Then $mPEG_{2k}$-NH_2 (0.05 mmol) dissolved in 1 mL of DMSO and trimethylamine (0.15 mmol) were added into the mixture. After 12 h stirring, the mixture was added to chloroform (CH_3Cl) and washed by 0.1 mol/L HCl and saturated NaCl solution. Then the organic layer was collected and removed by rotary evaporation. Then, methanol (MeOH) was introduced to precipitate unreacted bilirubin and the supernatants were collected and evaporated to obtain sticky solid. Small amount of chloroform was used to dissolve this solid and then precipitated in ether. The obtained solid was separated by silica gel column, with gradient elution of solution (CH_3Cl:MeOH) from 100:1 to 10:1. Finally, the collected liquid was removed by rotary evaporation and dried under high vacuum to obtain PEGylated bilirubin (PEG-BR) (yield: 65%). The product was characterized by matrix-assisted laser desorption/ionization time-of-flight mass spectrometry (Shimadzu, Japan).

For morpholine-decorated PEGylated bilirubin (M-PEG-BR), DIC (0.15 mmol), morpholin-4-yl-acetic acid hydrochloride (0.10 mmol), triethylamine (0.10 mmol) and DMAP (catalytic amount) were added into dimethylformamide (DMF) under a nitrogen atmosphere, and then the solution was stirred for 30 min. To this flask, a solution of DMF containing Fmoc-NH-PEG_{2k}-NH_2 (0.05 mmol) was added. The reaction solution was stirred at 30 °C for 2 days. Then, the solvent, catalyst, and unreacted raw material were mostly removed through dialysis with DMSO and water at room temperature. After dialysis, the solution was collected and lyophilized. The ^{1}H NMR results verified the successful conjugation of morpholine, otherwise the obtained product would continue to react. Fmoc groups were removed by the treatment with 20% (*v*/*v*) 4-methylpiperidine in dimethylformamide (DMF) for 30 min, and the PEGylated molecules were precipitated and washed three times by cold ether. Then, modifying bilirubin onto morpholine-decorated PEG was prepared as described previously (yield: 33%).

2.4. Loading of Ce6 and Dc to nanoparticles

A certain amount of Dc and Ce6 in a mixed solution ($CHCl_3$:MeOH = 3:1; 20 and 5 mg/mL, respectively) were introduced and mixed with 4 mg of PEG-BR or M-PEG-BR dissolved in 100 μL of $CHCl_3$. Then, 1.5 mL of water was added into the mixture, and then emulsified by using ultrasonic cell crusher (65 W, 5 s/5 s a cycle for 5 min). Centrifugation and ultrafiltration by KDC-140HR high speed refrigerated centrifuge (Anhui USTC Zonkia, China) were employed for the removal of free drugs and large particles to obtain Dc&Ce6@BNP or MBNP. The content of Ce6 was measured at an excitation/emission wavelength of 405/660 nm by a RF-5301PC spectrofluorophotometer (Shimadzu, Japan). And Dc was detected by high performance liquid chromatograph (HPLC) analysis, using a C-18 chromatography column (5 μm, 4.6 mm × 250 mm), and the separation conditions of elution were as follows: methanol:5% acetic acid aqueous solution (80:20); flow rate, 1.0 mL/min; and the detection wavelength was 276 nm.

2.5. Cellular uptake

When 4T1 cells were seeded into 6-well plates (3×10^5 cells per well) and grew to 80%, concentrated Cou6@BNP and Cou6@MBNP were diluted using fresh pH 7.4 or 6.5 medium without FBS and added into the wells at the same Cou6 concentration of 150 ng/mL, respectively. At 0.5 h and 2 h post incubation, the cells were collected and detected by flow cytometry (Agilent NovoCyte, USA). For a qualitative assay, 4T1 cells were plated into the coverslip in 6-well plates and treated with the same method as described above. Then, the cells were fixed with 4% paraformaldehyde and stained with DAPI. The fluorescence intensity was observed by confocal microscopy (A1R+, Nikon, Japan).

2.6. In vitro cytotoxicity assay

4T1 cells were cultured in the 96-well plates for 12 h. Then, the fresh pH 7.4 or 6.5 medium (as a control) or medium containing different formulations (Ce6+Laser, Dc, Dc&Ce6+Laser, Dc&Ce6@BNP, Dc&Ce6@BNP + Laser, Dc&Ce6@MBNP, and Dc&Ce6@MBNP + Laser) were introduced into wells. The irradiation was performed 8 h post incubation. After 24 h, the cytotoxicity was evaluated by MTT assay.

2.7. Apoptosis assay

4T1 cells were treated with pH 6.5 medium containing Ce6+Laser, Dc, Dc&Ce6@BNP + Laser and Dc&Ce6@MBNP + Laser (5 μg/mL for Ce6 and 17.5 μg/mL for Dc). Laser irradiation was conducted after 8 h. After 12 h, the cells were collected and stained with annexin V-FITC and PI, and measured by flow cytometry (BD FACSCelesta, USA).

2.8. Calcein-AM/PI staining assay

4T1 cells were cultured in 24-well plates as described above. Following different treatments for 24 h, cells were stained with calcein-AM (5 μg/mL) and PI (10 μg/mL). Then, cells were washed with PBS buffers to remove excessive dyes and imaged by fluorescence microscope.

2.9. Western blotting analysis

To start with, 4T1 cells were collected after the treatment with PBS, Ce6+Laser, Dc&Ce6+Laser, Dc&Ce6@BNP + Laser and Dc&Ce6@MBNP + Laser for 36 h (pH 6.5). The tumor tissues were harvested after four-times injection with PBS, Ce6+Laser, Dc&Ce6+Laser, Dc&Ce6@BNP + Laser and Dc&Ce6@MBNP + Laser. Then, lysis buffer was used to prepare the total cellular and tumor tissues proteins, followed by quantification using a BCA kit (Beyotime, Shanghai, China), according to the manufacturer's instructions. After the separation on SDS-

polyacrylamide gels and protein transfer to a PVDF membrane (Millipore, USA), the proteins were incubated overnight at 4 °C, with antibodies against rabbit LDHA (abclonal, China), rabbit HIF-1α (Abcam, UK), rabbit MCT1 (Thermo Fisher, US), rabbit CD31 (Servicebio, China), rabbit VEGFα (Abclonal, China) or rabbit angiopoietin-2 (Abclonal, China). After washing, membranes were treated with the second antibody (Abclonal, China) at 37 °C for 2 h, and then imaged using the enhanced chemiluminescence (ECL) method. Experiments were performed in triplicate.

2.10. *Immunofluorescence of cellular HIF-1α expression and LDHA expression under hypoxia*

4T1 cells were seeded onto coverslips and when cells grew to approximately 70%, and then incubated with drugs and formulations and covered with a layer of liquid paraffin to prevent oxygen entry for 24 h. Twelve hours post incubation, laser irradiation (80 mW/cm^2, 1 min) was conducted. After the liquid paraffin layer was quickly removed, paraformaldehyde was added to fix cells for 20 min. The process demanded rapid operation to minimize HIF-1α degradation. Then, the coverslips were washed and stained with anti-HIF-1α or anti-LDHA primary antibody at 4 °C overnight and then incubated with Alexa Fluro 647-labeled secondary antibody at 37 °C for 2 h. The nuclei were stained with DAPI. The stained cells were observed by CLSM.

2.11. *pH and lactate measurement*

For pH measurement, cells were cultured in 24-well plates. After 24 h incubation, 2 mL of fresh medium containing different formulations were added into the cells, along with pH detection at 0, 1, 2, 4, 8, 12, 24, 36 and 48 h. For lactate measurement, cells were seeded into 12-well plates for 24 h, and then incubated with different formulations for 48 h. The supernatant was collected and centrifuged to be determined with a lactate detection kit, and calibrated by BCA protein assay.

2.12. *Biodistribution*

4T1 cells (3×10^5 cells) were transplanted into the left mammary fat pad of female BALB/c mice. After 10 days, DiD@BNP and DiD@MBNP (0.3 mg DiD/kg) were intravenously injected into 4T1-bearing BALB/c mice. At 2, 6, 12 and 24 h, the fluorescence distribution was observed by the Lumina III Imaging System (PerkinElmer, USA). Twenty-four hours post injection, main organs were excised for imaging. Then, all the tumors and organs were dehydrated and frozenly sectioned to a 10 μm thickness with the freezing microtome (Leica CM1950, Germany). The DiD distributions were observed using a confocal microscope (A1R+, Nikon, Japan).

2.13. *In vivo anti-tumor test*

4T1 cells (3×10^5 cells) were transplanted into the left mammary fat pad of female BALB/c mice. Eight days later, when the tumor size reached around 70−80 mm^3, the mice were randomly divided into 8 groups ($n = 6$). Mice were intravenously injected with different formulations, including PBS, Ce6+Laser, Dc, Dc&Ce6+Laser, Dc&Ce6@BNP, Dc&Ce6@BNP + Laser, Dc&Ce6@MBNP, and Dc&Ce6@MBNP + Laser (3 mg/kg for Ce6 and 10.5 mg/kg for Dc), respectively. The irradiation was carried out 12 h post administration (150 mW/cm^2, 5 min). The treatments were repeated every 3 days for 4 cycles, while tumor volumes and body weights were recorded every 2 days. The tumor volumes were calculated with the following Eq. (1):

$$V = 0.5 \times \text{Length} \times \text{Width}^2 \quad (1)$$

After the last treatment, all the mice were sacrificed and major organs coupled with tumors were harvested. Part of them were fixed at 4% paraformaldehyde and used for H&E staining, Immunohistochemistry (CD31 staining) and Immunofluorescence staining (LDHA and TUNEL staining), and then imaged by microscope. The rest were used for Western blotting and lactate detection.

2.14. *Statistical analysis*

One-way analysis of variance (ANOVA) or *t*-test for multiple comparisons were used for statistical analysis. All data were expressed as mean ± standard deviation (SD). Statistical significance was set at $^*P < 0.05$, $^{**}P < 0.01$ and $^{***}P < 0.001$.

3. Results and discussion

3.1. *Preparation and characterization of Dc&Ce6@MBNP*

To start with, two types of materials, including morpholine-decorated PEGylated bilirubin (M-PEG$_{2K}$-BR) and PEGylated bilirubin (PEG$_{2K}$-BR), were synthesized (Fig. 2A and Supporting Information Scheme S1) and confirmed by matrix-assisted laser desorption/ionization time of flight mass spectrum (MALDI-TOF-MS). The peaks at *m/z* around 2073 and 2676 in Supporting Information Fig. S1, 2090 and 2648 in Supporting Information Fig. S2 belonged to MeO-PEG$_{2K}$−NH$_2$, PEG$_{2K}$-BR, Fmoc-NH-PEG$_{2K}$-NH$_2$, M-PEG$_{2K}$-BR, respectively, while proton nuclear magnetic resonance (^{1}H NMR) spectra showed the appearance of characteristic peak of bilirubin, including HC═CH$_2$ and HC═C proton signal at 5−7 ppm, in PEG$_{2K}$-BR and M-PEG$_{2K}$-BR, indicating the successful linkage of bilirubin to PEG (Supporting Information Figs. S5 and S6). Meanwhile, ^{1}H NMR spectra directly demonstrated the morpholine groups were successfully conjugated to Fmoc-NH-PEG$_{2K}$-NH$_2$, as (CH$_2$)$_2$N proton signal appeared roughly at 2.6 ppm (Fig. S6). The morpholine group in Fmoc-NH-PEG$_{2K}$-M were further verified by the appearance of the absorption peak at 1677 cm^{-1} ($\nu_{C=O}$) in near-infrared (IR) spectra, while peak of C═O group in raw material (Fmoc-NH-PEG$_{2K}$-NH$_2$) only located in 1718 cm^{-1} (Supporting Information Fig. S3). After the removal of Fmoc, the remaining M-PEG$_{2K}$-NH$_2$ only showed peak at 1677 cm^{-1}, rather than 1718 cm^{-1}. Coupled with the UV−Vis spectra of raw and synthesized materials (Supporting Information Fig. S7), these above demonstrated that compound morpholine and bilirubin have successfully conjugated onto the N terminus of PEG.

In an aim to achieve both optimal synergism between drugs and preferable drug loading, the *in vitro* cytotoxicity of different masses of free Dc and Ce6 was firstly evaluated in 4T1 cell lines, as the combination indexes (CI), simulated from cell viability curves (Fig. 2B), was introduced to assess the synergism. As shown in Fig. 2C, three mass ratios all were below this dotted line (CI = 1), indicating the notable synergistic effects between Dc and Ce6 among these ratios. When the mass ratio reached 1:2, the fact that CI values was the lowest displayed better combination

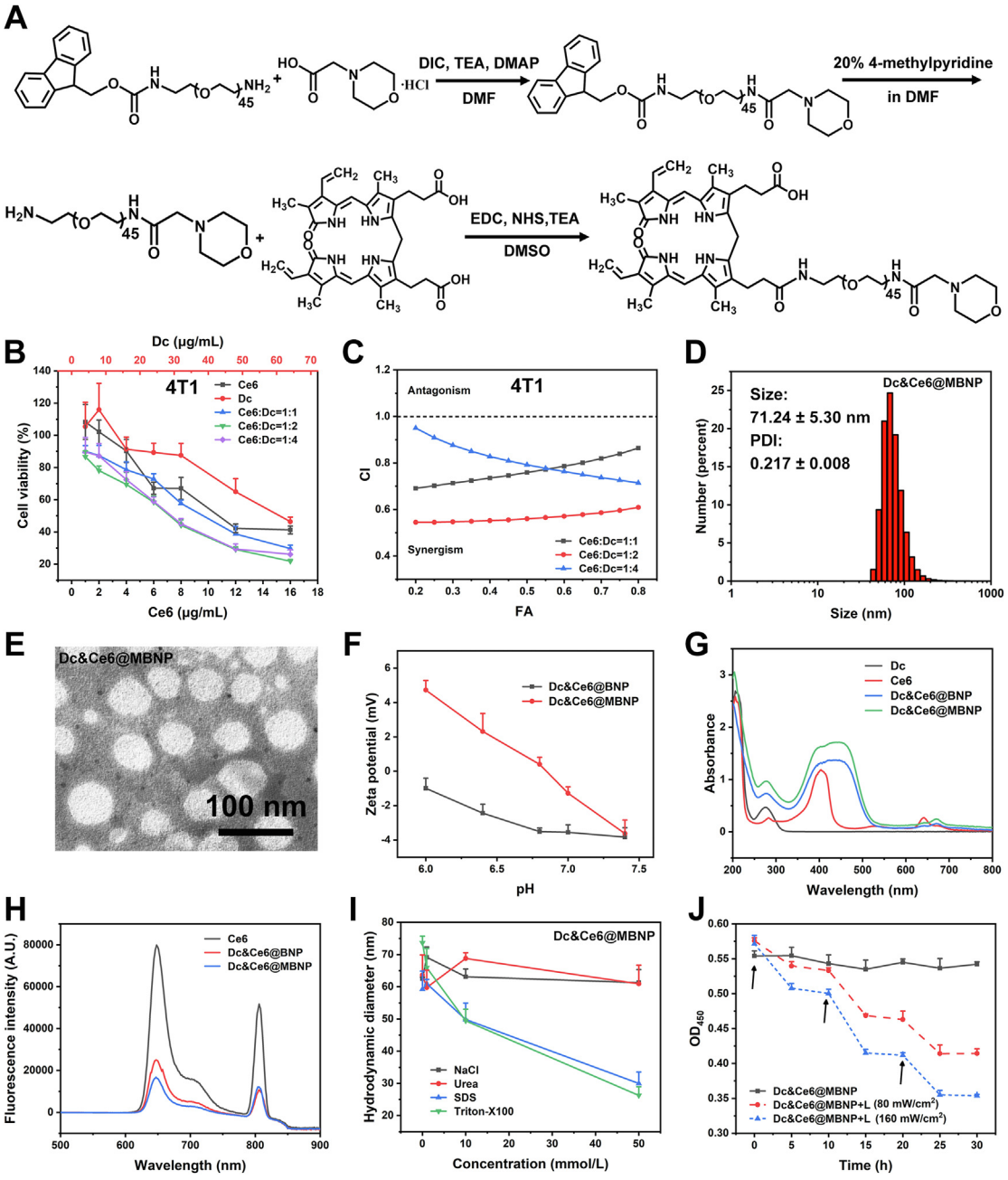

Figure 2 Characterizations of Dc&Ce6@MBNP. (A) Synthesis route of M-PEG_{2K}-BR. (B) *In vitro* cytotoxicity of free Ce6 and Dc on 4T1 cells. (C) CI value simulated from (B) using CalcuSyn software. (D) Size distribution and (E) typical TEM image of Dc&Ce6@MBNP. (F) Changes of zeta potentials of BNP and MBNP in PBS at different pH values from 6.0 to 7.4 ($n = 3$, mean ± SD). (G) UV−VIS absorption spectra of free Dc, free Ce6 and NPs in PBS (pH = 7.4). (H) Fluorescence spectra of free Ce6 and NPs in PBS (pH = 7.4). (I) Hydrodynamic diameters of Dc&Ce6@MBNP upon addition of NaCl, urea, SDS and Triton X-100 ($n = 3$). (J) Changes in OD_{450} of Dc&Ce6@MBNP following treatments with different circles of laser irradiation ($n = 3$). Black arrows correspond to 2-min irradiation here.

outcomes. So we tried to load drugs at this mass ratio (1:2) into M-PEG_{2K}-BR and PEG_{2K}-BR. The Dc and Ce6-coloaded bilirubin nanoparticles (Dc&Ce6@BNP and Dc&Ce6@MBNP) were prepared by ultrasonic emulsification. When drug/polymer ratio reached 3:25, the encapsulation efficiencies of Dc and Ce6 in BNP were 87.54 ± 7.23% and 49.93 ± 2.06%, while the drug loading achieved 6.42 ± 0.57% and 1.83 ± 0.08%, respectively. By contrast, those in MBNP were 81.58 ± 6.78% and 46.90 ± 1.95%, while the loading capacities reached 6.02 ± 0.54% and 1.73 ± 0.07%. The drug mass ratios in two NPs approximately exhibited 3.51 and 3.48, respectively. Although the mass ratio (~3.5) was less optimal for synergism, the nanoparticles with an overall drug loading capacity (~8%) was sufficient to satisfy the demand of treatment.

The average size of Dc&Ce6@BNP and Dc&Ce6@MBNP was 68.04 ± 16.92 and 71.24 ± 5.30 nm, respectively (Supporting Information Fig. S8A and Fig. 2D), which was determined by the dynamic light scattering (DLS) analysis. The size distributions of

both nanoparticles were narrow, as indicated by polydispersity index (PDI) less than 0.3. Transmission electron microscope (TEM) results showed two nanoparticles presented a round shape with a size of approximately 70 nm, consistent with the above DLS data (Fig. S8A and Fig. 2E). UV spectra revealed the co-assembled NPs in PBS had the typical absorbance peaks from PEG-bilirubin (450 nm), Dc (276 nm) and Ce6 (405 and 650 nm). This indicated these three components interacted with each other and constructed the nanoparticles at nanoscale (Fig. 2G). A considerably broader and red-shifted Soret band of Ce6, plus a slightly red-shifted absorption band of Dc, implied that the pyrrole groups of bilirubin could interact with aromatic ring of Dc and pyrrole groups of Ce6 by hydrophobic interactions and $\pi-\pi$ stacking[42]. Besides, the interaction of Ce6 with PEG-BR and Dc was evaluated by fluorescence as well. The intrinsic fluorescence of emission peaks of Ce6 (650 nm) after encapsulated inside NPs was remarkably decreased compared to monomeric Ce6 (Fig. 2H). The significant fluorescence quenching has reportedly been ascribed to the formation of $\pi-\pi$ stacking inside polymeric NPs[42,43]. Apart from the above, we also introduced SDS, Triton X-100, NaCl and urea into as-obtained nanoparticles, in an aim to observe the impact on their structure by size measurements[44,45]. Dc&Ce6@BNP and Dc&Ce6@MBNP didn't show any size reduction in NaCl and urea, while the addition of SDS and Triton X-100 caused obvious size reduction (Fig. S8B and Fig. 2I), proving that hydrophobic interactions, instead of electrostatic interaction, played a dominant role in the formation of nanoparticles. As a result of those associative forces inside NPs, including hydrophobic and $\pi-\pi$ interaction, both BNP and MBNP retained a good stability in the aqueous state for 48 h. Any significant change of size and PDI was hardly observed in both groups (Fig. S8C).

Of note, the main difference between MBNP and BNP was the modification of morpholine group, so zeta potentials of MBNP and BNP under different pH were determined (Fig. 2F). As expected, the zeta potential of MBNP converted from near neutral to positive (4.7 mV), when pH decreased from 7.4 to 6.0. By comparison, BNP still remained near neutral (-1.0 mV)[36]. This suggested the MBNP's ability of charge reversal. On the other hand, owing to the presence of bilirubin in the hydrophobic core, this nanocarrier also possessed ROS responsiveness (Supporting Information Fig. S10). DLS data showed exposure to 5-min laser light could decrease the count rate of drug-loaded NPs in water by close to half, which was proportional to the number of NPs (Supporting Information Table S1). As seen in Fig. S8F and Supporting Information Fig. S9B, ROS generation upon laser exposure could transform yellowish bilirubin into hydrophilic biliverdin and photoisomers, with a characteristic greenish color. Moreover, upon the first 2 min of irradiation, a notable decrease in the absorbance at 450 nm (OD_{450}) was observed, which mirrored bilirubin concentration, as depicted in Fig. S8D and Fig. 2J. With the laser power or irradiation cycles increasing, OD_{450} dropped more sharply, while NPs without irradiation almost remained constant during the same procedure. As a control, without Ce6, Dc@BNP and Dc@MBNP can hardly respond to multiple cycles of laser irradiation, as OD_{450} still kept approximately the same (Figs. S8E and S9A). The results altogether demonstrated large amounts of ROS produced by Ce6 upon 650 nm irradiation, irrespective of irradiation itself, could sufficiently result in the collapse of BNP and MBNP. Based on this, we further delved into the laser-triggered drug release from nanoparticles. From Supporting Information Fig. S11, upon laser illumination (160 mW/cm^2), Dc&Ce6@BNP released more than 49.49% of Dc within 1 h, while approximately 49.13% of Dc was released from Dc&Ce6@MBNP. With time extended to 48 h, both nanoparticles released more than 80% of Dc upon laser irradiation. By contrast, at 48 h time point, only 40% of Dc release was observed in corresponding groups without laser irradiation, which was favorable for controllable drug delivery. Taken together, this nanocarrier possessed a charge-switchable property and ROS-responsive drug release profile.

3.2. *Charge reversal-mediated endocytosis and ROS production*

Encouraged by the transition in zeta potential of MBNP, we surmised this charge reversal could facilitate the cellular uptake of nanoparticle at acidic pH. Coumarin 6 (Cou6) was chosen as a fluorescent probe to detect the endocytosis in 4T1 cells. Flow cytometry results showed MBNP and BNP exhibited similar fluorescent intensity of Cou6 at pH 7.4 for 0.5 and 2 h (Fig. 3A). Predictably, the intensity of MBNP at pH 6.5 for 0.5 h was 1.24- and 1.19-fold higher than that of BNP at pH 6.5 and MBNP at pH 7.4, respectively. Additionally, the intensity of MBNP at pH 6.5 for 2 h was 1.44- and 1.33-fold higher, compared with BNP at pH 6.5 and MBNP at pH 7.4. Likewise, the results in confocal imaging indicated the fluorescent intensity of Cou6 in MBNP at pH 6.5 was significantly stronger than BNP at pH 6.5 and MBNP at pH 7.4 (Fig. 3B and Supporting Information Fig. S12A), in accordance with previous research[35,36]. All the evidence strongly supported desirable targeting ability of morpholine-decorated nanocarriers towards tumor cells at acidic microenvironment.

After specific internalization by malignant cells, ROS generation by Ce6 in different formulations was examined by flow cytometry as well. 2′,7′-dichlorodihydrofluorescein diacetate (DCFH-DA) was employed as an ROS indicator, which could transform to dichlorofluorescein with green fluorescence upon exposure to ROS. 4T1 cells were treated with different formulations for 4 h, followed by incubation with DCFH-DA for 30 min and washed twice. Then, 650 nm laser irradiation was conducted for 1 min (80 mW/cm^2). From the Fig. 3C, irradiation could trigger abundant ROS production in all but control group and Dc, whether at pH 7.4 or 6.5. In addition, a degree of fluorescence increase were observed in the corresponding group without irradiation, particularly Ce6 group, compared with control group. The fluorescent intensity of Ce6-encapsulated NPs were always lower than free Ce6. Interestingly, when exposed to irradiation, Ce6 resulted in the highest ROS level, successively followed by Dc&Ce6@MBNP, Dc&Ce6@BNP and Ce6@BNP at pH 6.5, while negligible variations were found among different NPs at pH 7.4. The phenomenon might arise from ROS-scavenging property of bilirubin nanoparticles or different cell entry efficiencies between free Ce6 and NPs. Taken together, Dc&Ce6@MBNP gained an enhanced cellular uptake and drug release profile in respond to ROS.

3.3. *Effects on LDHA expression, lactate secretion and acidity alleviation in vitro*

As mentioned earlier, LDHA is typically upregulated in cancers, as a result of accelerated glycolysis of cancer cells especially under hypoxia, whereas LDHB has opposite effects on metabolism. Besides, c-MYC and HIF-1α promote breast cancer tumorigenesis at least in part through the induction of aerobic glycolysis by promoting transcription of key glycolytic enzymes,

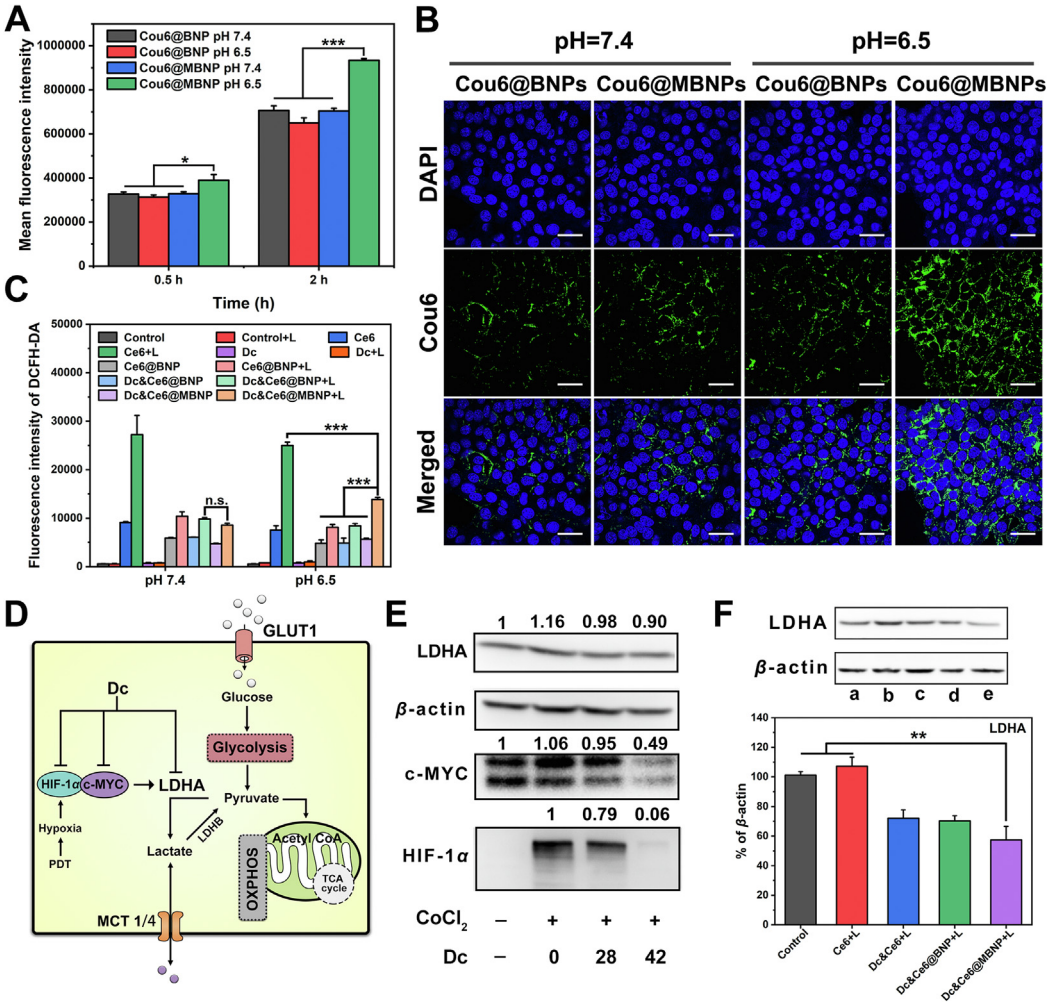

Figure 3 Cellular uptake, ROS generation and lactate modulation *in vitro*. (A) Flow cytometry results of endocytosis of Cou6@BNP and Cou6@MBNP at pH 7.4 and 6.5 for 0.5 and 2 h ($n = 3$, mean ± SD, $^{*}P < 0.05$, $^{**}P < 0.01$, $^{***}P < 0.001$). (B) Confocal images of the cellular uptake of Cou6@BNP and Cou6@MBNP at pH 7.4 and 6.5 for 2 h. Blue indicates the cell nucleus. Green indicates Cou6. Scale bars represent 50 μm. (C) ROS generation in various formulations at cell level measured by flow cytometry. (D) Schematic illustration of mechanism of synergistic hypoxia-targeted photodynamic therapy through regulating LDHA. (E) Western blotting analysis of HIF-1α, c-MYC and LDHA expression treated with $CoCl_2$ and different concentrations of Dc in 4T1 cells at pH 7.4 for 24 h. (F) Western blotting and semi-quantitative analysis of LDHA expression in 4T1 cells treated with different formulations upon irradiation (80 mW/cm^2, 1 min) at pH 6.5 for 36 h ($n = 3$, mean ± SD, $^{*}P < 0.05$, $^{**}P < 0.01$, $^{***}P < 0.001$). The a−e in (F) represent control, Ce6+L, Dc&Ce6+L, Dc&Ce6@BNP + L and Dc&Ce6@MBNP + L.

such as LDHA[46]. Based on this, LDHA, LDHB and c-MYC expression in different malignant and normal cells were evaluated and compared (Supporting Information Fig. S14). Although LDHA expression of 4T1 was lower, it should be noted that the LDHA/LDHB ratio was remarkably elevated relative to B16F10 (melanoma cells), MCF-7 (human breast cancer cells) and HUVEC (human umbilical vein endothelial cell; normal cells). This result implied that HUVEC and MCF-7 relatively depended on OXHOPS, while 4T1 and B16F10 were more inclined to glycolysis, which was consistent with the results assessed by extracellular acidification rate and oxygen consumption rate found in previous studies[34,47]. Meanwhile, the expression of oncoprotein c-MYC was highest in 4T1 cells, while it was also found to be enhanced in other cancer cells, compared with HUVEC. Furthermore, the combination of free Dc and Ce6 were investigated in MCF-7, B16F10 and HUVEC by MTT assay. The synergism between Dc and Ce6 were demonstrated in B16F10 and HUVEC, but slight combined effects was found in oxidative MCF-7 (Supporting Information Fig. S20). By contrast, highly glycolytic 4T1 cells were more sensitive to relatively lower concentrations of Dc (Fig. 2B).

Since Dc was reported to act on LDHA[18,20,48], we firstly assessed the influence of free Dc on LDH activity. As shown in Supporting Information Fig. S13, with concentrations increasing to 28 μg/mL, free Dc displayed significantly stronger inhibitory effects on LDH activity, compared to control groups. But 42 μg/mL Dc abated this inhibition, partly due to the impact of a portion of cell death by Dc. Additionally, LDH activity was decreased to at most 13.21%, during 24-h treatment. So, the focus was shifted into the influence of Dc on LDHA expression.

Western blotting assay was employed to study LDHA protein expression. 4T1 cells were firstly incubated with free Dc of fixed

concentration (28 μg/mL) for 12, 24, 36 or 48 h at pH 7.4. The downregulation was incremental over time, as 24 or 36 h reduced 12% or 27% of LDHA expression, but until 48 h, it still remained about 26% reduction (Supporting Information Fig. S15A)[48]. Besides, when $CoCl_2$, one of HIF-1α inducers, was added into medium, enhanced level of LDHA was observed, compared with control group, suggesting LDHA expression was partly regulated by HIF-1α, consistent with previous study. After the addition of Dc, decreased level of LDHA was also found and interestingly, HIF-1α expression was greatly reduced to 82.25% at 28 μg/mL and 9.89% at 42 μg/mL (Fig. 3E), reported in previous literature[33]. For c-MYC, $CoCl_2$ treatment increased slightly its expression, while Dc could markedly block its expression with concentration increase to 42 μg/mL (Fig. 3E)[18]. In addition, the impact of Dc on LDHA, c-MYC and HIF-1α in other cells, after $CoCl_2$ treatment, were also assessed, as exhibited in Supporting Information Figs. S17−S19. Dc could reduce c-MYC and HIF-1α expression, but LDHA decrease were found in B16F10 and HUVEC, rather than MCF-7. It might result in the stiff resistance of MCF-7 towards Dc.

Then, we continued to investigate the effects of Dc-containing formulations on LDHA expression at pH 6.5. As shown in Fig. 3F, the expression of LDHA was not affected and instead raised slightly by the incubation with Ce6+L group (also shown in Fig. S15B). But, the incorporation of Dc led to varying degrees of blockade, as LDHA expression was remarkably reduced to 72.08 ± 5.65%, 70.18 ± 3.52% or 57.38 ± 9.18% after cells treated with Dc&Ce6+L, Dc&Ce6@BNP + L or Dc&Ce6@MBNP + L (equivalent to 28 μg/mL Dc), respectively. Plus, these groups without irradiation were evaluated to confirm that decrease of LDHA expression was ROS-dependent. In Fig. S15C, Dc&Ce6 reduced its expression to 66.91 ± 6.12%, while Ce6, Dc&Ce6@BNP and Dc&Ce6@MBNP reduced to 93.26 ± 3.33%, 92.80 ± 8.18% and 82.91 ± 2.09%, respectively. Based on these obtained results, we continued to evaluate the impact of Dc and different formulations on HIF-1α and LDHA expression under hypoxia by immunofluorescence (owing to the rapid degradation of HIF-1α under normoxia). Upon irradiation, higher fluorescent intensity of HIF-1α were observed in Ce6 and Ce6@BNP, while the introduction of Dc could alleviate hypoxia through decreasing HIF-1α expression (Supporting Information Fig. S16A). The fluorescent intensity of Dc&Ce6@MBNP + L was lower than Dc&Ce6@BNP + L, at least partly due to charge reversal-enhanced endocytosis at pH 6.5. Likewise, the decreasing trend of LDHA expression under hypoxia were also found in Dc&Ce6@BNP + L and Dc&Ce6@MBNP + L (Fig. S16B).

After the expression of LDHA was depressed, the end product-lactate production would be inhibited as well. Upon Dc exposure for 48 h, the concentrations of lactate in the cell culture media decreased from 0.19 to 0.13 mg/mL, while little variation in extracellular lactate was observed in Ce6+L group (Fig. S12B). Strikingly, Dc&Ce6@MBNP + L treatment reduced lactate secretion of 4T1 cells to a maximum of 60%, in parallel to Dc&Ce6@BNP + L (30%), as a result of charge-reversal enhanced internalization. It should be pointed out that the suppressed lactate secretion was not due to reduced cell viability, which was normalized by BCA protein assay. Similarly, Dc increased pH in the supernatants of 4T1 cells, whereas Ce6 treatment had no effect on this (Fig. S12C). Other Dc-containing formulations also caused the elevation in pH to 7.2, which was consistent with the reduction in lactate secretion. LDHA blockade in 4T1 cells was a part of reason why Dc decreased lactate secretion and alleviated pH, because other studies demonstrated Dc could block the activity of lactate transporters MCT-1 and MCT-4[34,48]. Regardless of free drug or formulations, Dc could, to an extent, reduce LDHA activity and expression by regulating c-MYC and HIF-1α expression in 4T1 cells, coupled with decreased lactate secretion and elevated extracellular pH (Fig. 3D).

3.4. *In vitro cytotoxicity studies*

To further corroborate the synergistic anti-tumor efficacy, various methods were adopted to study the *in vitro* cytotoxicity after different treatments. The methyl thiazolyl tetrazolium (MTT) assay was firstly introduced. Different concentrations of the blank nanoparticles without drug (BNP and MBNP) didn't exhibit any toxicity towards HUVEC (Supporting Information Fig. S21B) and 4T1 cells (Fig. S21A), regardless of at pH 7.4 or 6.5. This could exclude the possible effect of solution pH and concentrations of nanoparticles on cell viability and indirectly confirm the biosafety and biocompatibility of nanomaterials. It is known that tumor cell proliferation correlates with upregulated expression of oncogene like c-MYC and that c-MYC inhibition can revert the neoplastic phenotype and induce apoptosis[49]. Dc suppressed the growth of 4T1 cells, partly due to its inhibition on c-MYC and LDHA. As described in Fig. 4B, Ce6&Dc group upon 20 s irradiation (80 mW/cm^2) showed obvious cytotoxicity, particularly when the Ce6 concentration increased to 8 μg/mL. Compared with free Dc (IC_{50} = 45.26 μg/mL) or Ce6 (IC_{50} = 12.84 μg/mL) alone, the combination of Dc and Ce6 showed a half maximal inhibitory concentration (IC_{50}) of 7.392 μg/mL, which was attributable to the synergy. After loaded into nanoparticles, the IC_{50} of Ce6@BNP + L increased to 15.02 μg/mL, largely due to the attenuation of ROS stress by bilirubin. Meanwhile, limited cytotoxicity was observed in Ce6@BNP, Dc&Ce6@BNP and Dc&Ce6@MBNP without laser, while only 13.74%, 28.3% and 31.23% cell death were detected at the highest concentration. Relative to Dc&Ce6@BNP + L (9.02 μg/mL), the Dc&Ce6@MBNP + L group displayed higher cytotoxicity at pH 6.5 (5.90 μg/mL), which might be ascribed to the enhanced endocytosis of the Dc&Ce6@MBNP in acidic milieu. Simultaneously, the cytotoxicity of Dc&Ce6@BNP + L still remained unchanged from pH 7.4 to 6.5, while Dc&Ce6@MBNP + L showed higher cytotoxicity at pH 6.5 relative to pH 7.4 (Fig. 4C, Figs. S21C and S21D). These data jointly indicated the anti-tumor effects were enhanced by the synergy of Dc and Ce6, and subsequently by morpholine-mediated increased uptake. Under hypoxia, Ce6 upon irradiation were less likely to induce cell death than that under normoxia, which implied low oxygen level could limit its efficacy, while Dc restored tumor sensitivity towards PDT under hypoxia, as its addition still greatly increased PDT's toxicity towards 4T1 cells (Supporting Information Fig. S22).

For more intuitive observation of anti-tumor effect *in vitro*, calcein-AM/PI double staining was applied to mark off live cells and late apoptosis/dead cells (Fig. 4A). All cells were alive without laser illumination at pH 6.5, and the cells incubated with free Ce6, rather than free Dc and Dc&Ce6, resembled the control group. Negligible changes were found in Dc&Ce6@BNP and Dc&Ce6@MBNP without irradiation. Upon irradiation, cells died in different extents. Ce6 caused enormous dead cells, but lower than dual drug combination, highlighting the synergistic effect of Dc and Ce6. Dc&Ce6@MBNP resulted in almost all the cell death upon irradiation, demonstrating the desirable therapeutic efficacy of charge-reversal mediated combination therapy.

In addition, the cell apoptosis was evaluated by annexin V-FITC and PI double staining assay (Fig. 4E). The concentration of Dc and Ce6 was lowered to 17.5 and 5 μg/mL, in comparison to the usage for

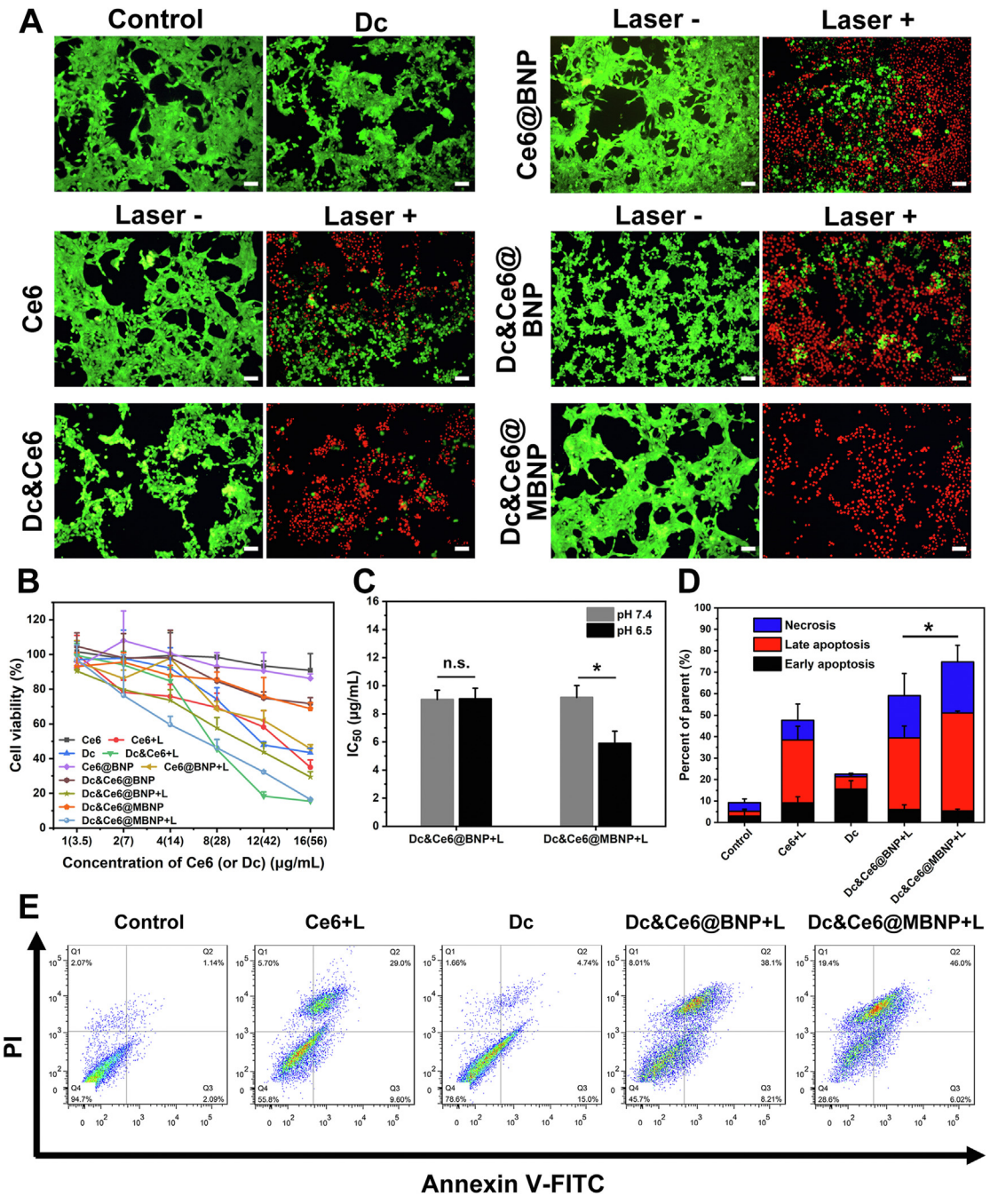

Figure 4 *In vitro* cytotoxicity assays. (A) Calcein-AM/PI double staining of cells at pH 6.5 after different treatments. Scale bars represent 100 μm (laser: 650 nm, 80 mW/cm^2, 1 min). (B) 4T1 cells viability treated with different formulations at pH 6.5 for 24 h, measured by MTT assay (laser: 650 nm, 80 mW/cm^2, 20 s). (C) The IC_{50} of Dc&Ce6@BNP + L and Dc&Ce6@MBNP + L at pH 7.4 and 6.5 ($n = 3$, mean ± SD, $^*P < 0.05$, $^{**}P < 0.01$, $^{***}P < 0.001$; n.s., not significant). (D) Quantitative comparison and (E) apoptosis analysis of cells at pH 6.5 after different treatments by flow cytometry (laser: 650 nm, 80 mW/cm^2, 1 min; $n = 3$, mean ± SD, $^*P < 0.05$, $^{**}P < 0.01$, $^{***}P < 0.001$).

calcein-AM/PI staining. Free Dc alone induced 15.57 ± 3.88% of early apoptotic cells and 5.79 ± 0.91% of late apoptotic cells, while free Ce6 upon irradiation also elicited 9.24 ± 7.54% of necrotic cells, as well as 9.13 ± 2.84% and 29.27 ± 6.40% of cells in early and late apoptotic stage, respectively. In parallel to Dc&Ce6@BNP + L, Dc&Ce6@MBNP + L triggered 1.27-fold more cells in apoptotic and necrotic stage at pH 6.5 (Fig. 4D). These findings indicated enhanced cellular uptake by morpholine led to better therapeutic response against tumor cells.

3.5. *In vivo pharmacokinetics and biodistribution analysis of the nanocarriers*

The excellent *in vivo* tumor-targeted accumulation was the basic premise of nanocarriers to achieve superior anti-tumor response. Before the investigation of *in vivo* distribution, the pharmacokinetics profiles of different formulations were evaluated by fluorescence quantitatively. 1,1-Dioctadecyl-3,3,3,3-tetramethylindodicarbocyanine perchlorate (DiD), a hydrophobic

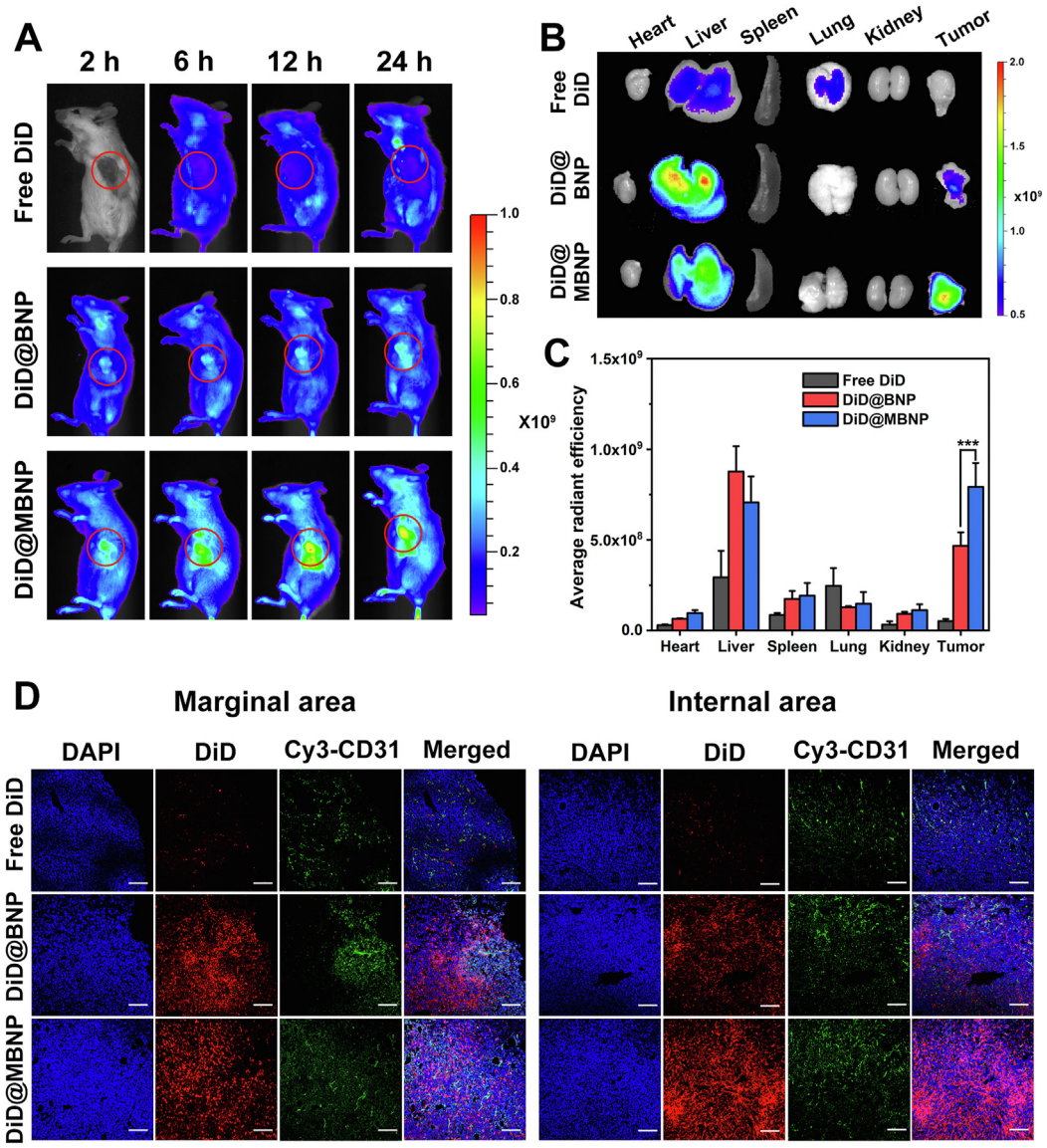

Figure 5 *In vivo* biodistribution of nanocarriers. (A) *In vivo* imaging of DiD-loaded formulations in 4T1 tumor-bearing mice at different times post administration. Tumor sites are marked by red circles. (B) *Ex vivo* imaging of isolated tumors and organs from mice after 24 h. (C) Semi-quantification of fluorescence intensity ($n = 3$, mean ± SD, $^{*}P < 0.05$, $^{**}P < 0.01$, $^{***}P < 0.001$). (D) Fluorescent distribution of Free DiD, DiD@BNP and DiD@MBNP in the frozen sections of tumors. Blue indicates the cell nucleus. Red indicates DiD. Green indicates CD31. Scale bars are 100 μm.

fluorescent agent, was encapsulated into BNP and MBNP for the following experiment. As displayed in Supporting Information Fig. S23 and Table S2, both DiD@BNP and DiD@MBNP had a relatively long blood circulation half time ($t_{1/2}$), which was longer than 13 h. Notably, DiD@MBNP enjoyed a higher $AUC_{(0-\infty)}$ than DiD@BNP, while the mean residence time ($MRT_{(0-\infty)}$) of MBNP was 23.54 ± 1.68 h, 1.17-fold longer than BNP group. The result implied morpholine modification could prolong the blood circulation time of nanoparticles.

In vivo fluorescence imaging indicated all the DiD-loaded formulations distributed in the whole body after intravenous injection for 2 h (Fig. 5A). At tumor sites, the fluorescence signals in DiD@MBNP was much stronger than that of DiD@BNP group and free DiD, regardless of time points post-injection. Moreover, the *ex vivo* imaging of isolated tumors after 24 h also exhibited the higher accumulation of DiD@MBNP group in tumor (Fig. 5B). Tumor tissues treated with DiD@MBNP showed 15.44- and 1.69-fold higher fluorescence intensity than that of free DiD and DiD@BNP, respectively (Fig. 5C). To clearly observe the distribution in tumor tissues, all tumors at 24 h were sliced and stained with CD31 antibody to mark the blood vessels, and the results were in concord with the *in vivo* imaging (Fig. 5D). While free DiD hardly appeared in the marginal or internal area of tumors, DiD@BNP and DiD@MBNP both showed strong fluorescent intensity in marginal area. Interestingly, the intensity of DiD@MBNP in internal area was much higher than that in marginal area, contrary to DiD@BNP, indicating most of BNP got trapped in periphery of tumors rather than penetrating into inner core, while MBNP possessed superb ability of tumor penetration. Altogether, these data strongly validated that morpholine

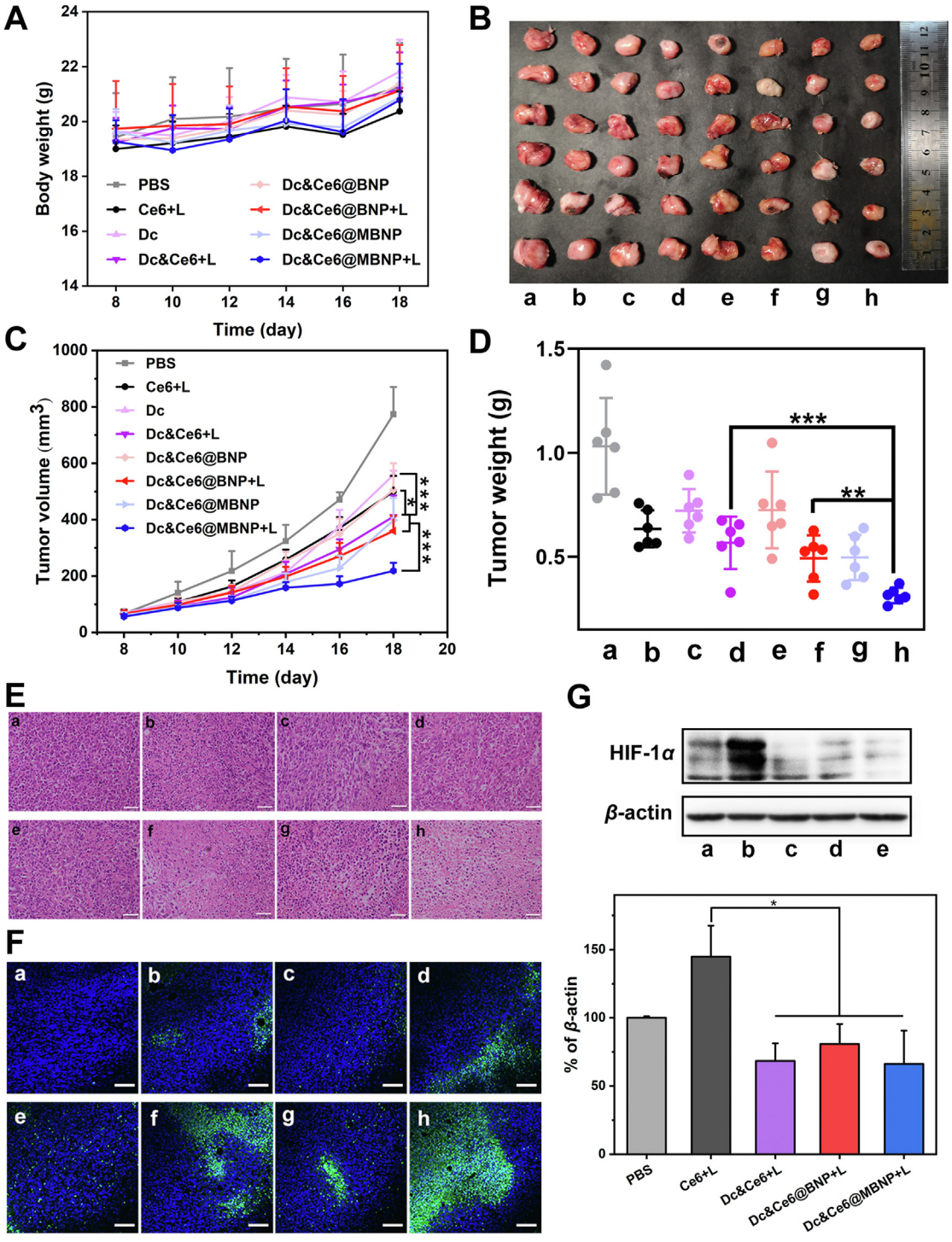

Figure 6 *In vivo* anti-tumor performance of different formulations. (A) Body weight and (C) 4T1 tumor growth curves of the mice after different treatment. (B) Photographs and (D) average weights of the isolated tumors on Day 20 ($n = 6$, mean ± SD, $^{*}P < 0.05$, $^{**}P < 0.01$, $^{***}P < 0.001$). (E) H&E and (F) TUNEL staining of the corresponding tumor sections. Scale bars (H&E) are 20 μm; scale bars (TUNEL) are 100 μm. The a−h in (B), (D), (E) and (F) represent PBS, Ce6+L, Dc, Dc&Ce6+L, Dc&Ce6@BNP, Dc&Ce6@BNP + L, Dc&Ce6@MBNP and Dc&Ce6@MBNP + L. (G) Western blotting analysis of HIF-1α protein expression from tumor tissues obtained after different treatments and the corresponding semi-quantitative results ($n = 3$, mean ± SD, $^{*}P < 0.05$, $^{**}P < 0.01$, $^{***}P < 0.001$).

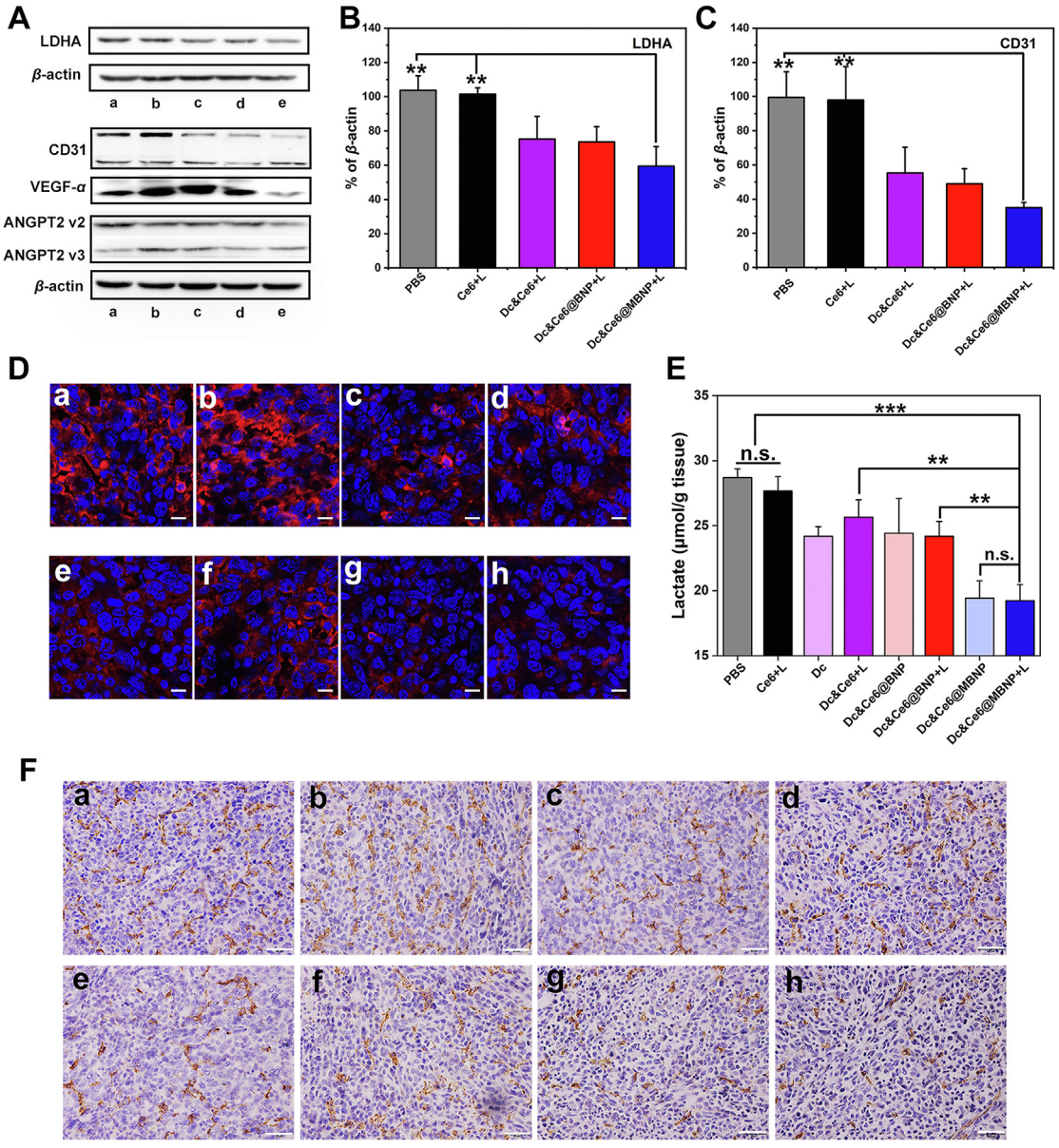

Figure 7 Lactate modulation-enabled TME alteration. (A) Western blotting analysis of LDHA and angiogenesis-related protein expression from tumor tissues obtained after different treatments. The a−e in (A) represent PBS, Ce6+L, Dc&Ce6+L, Dc&Ce6@BNP + L and Dc&Ce6@MBNP + L. (B) and (C) Semi-quantitative analysis of the ratio of LDHA and CD31 expressions to β-actin expression using ImageJ ($n = 3$, mean ± SD, $^{**}P < 0.01$, $^{***}P < 0.001$). (D) IF staining of LDHA and (F) IHC staining of CD31 in tumor sections. Scale bars (LDHA) represent 10 μm; Scale bars (CD31) represent 20 μm. (E) The concentrations of lactate in tumor tissues ($n = 3$, mean ± SD, $^{**}P < 0.01$, $^{***}P < 0.001$; n.s., not significant). The a−h in (D) and (F) correspond to PBS, Ce6+L, Dc, Dc&Ce6+L, Dc&Ce6@BNP, Dc&Ce6@BNP + L, Dc&Ce6@MBNP and Dc&Ce6@MBNP + L.

modification, in response to acidic microenvironment, could enable nanocarrier more prone to accumulate in tumor sites.

3.6. In vivo anti-tumor performance and lactate modulation-enabled TME alterations

The potential of Dc&Ce6@MBNP to curb tumor progression was carried out through a subcutaneous 4T1 breast cancer model. Since tumor grew to approximately 70 mm^3, mice were treated with 4 injections of various formulations, including PBS, free Ce6+L, free Dc, free Dc&Ce6+L, Dc&Ce6@BNP, Dc&Ce6@BNP + L, Dc&Ce6@MBNP and Dc&Ce6@MBNP + L. The tumor growth curves after different treatments were presented in Fig. 6C. Within 20 days, tumors of mice treated with phosphate buffer saline (PBS) rapidly grew over 770 mm^3, while the growth speed of tumors tended to get slightly slower in free Dc and free Ce6+L group. The combination, relative to free Ce6 (35.3%) or Dc alone (27.6%), resulted in an average tumor volume of around 410 mm^3 and 46.8% of tumor growth suppression (compared with the PBS group on Day 20), suggesting synergistic anti-tumor effects of Dc and Ce6. After being encapsulated into nanoparticles, the tumor volume decreased to 360 mm^3 and the

inhibition rate reached 53.5%, suggesting the nanoparticles could passively target tumor. Dc&Ce6@MBNP without irradiation also inhibited tumor growth to some extent, as a result of high ROS levels in tumor tissues, compared with *in vitro*. Furthermore, morpholine modification gave rise to better anti-tumor effect, as the Dc&Ce6@MBNP + L group led to 71.7% of tumor regression, which was 1.34- and 1.53-fold higher than that of Dc&Ce6@BNP and Dc&Ce6 upon irradiation. The apparently enhanced suppression was attributed to higher tumor targeting ability, exerted by the charge reversal of morpholine in response to acidity. The weights (Fig. 6D) and images of all resected tumors (Fig. 6B) were in line well with the measurement of tumor volumes. Most groups displayed higher weight (>0.5 g), while tumor weights of Dc&Ce6@MBNP + L were mainly distributed between 0.2 and 0.4 g, which was 1.57-, 1.81- and 3.28-fold higher than that of Dc&Ce6@BNP + L, Dc&Ce6+L and PBS group.

Besides, the body weights of all groups displayed slight increase within 20 days (Fig. 6A). Hematoxylin and Eosin (H&E) staining of main organs also implied negligible histological changes in different treatments (Supporting Information Fig. S25). When the mice were sacrificed, the blood samples were also obtained. Biochemical parameters showed that TBIL in the treatment groups, particularly BRNPs-treated ones, increased to a certain extent but within normal range compared with control groups, but there were no significant changes in other indicators of heart, kidney and liver function (Supporting Information Fig. S26). These evidences indicated no obvious toxicity was induced by formulations. The tumor apoptosis in different groups was further investigated by H&E (Fig. 6E) and TUNEL staining (Fig. 6F) of tumor tissues. More severe nuclei damages and cytosol degradations were observed in Dc&Ce6@MBNP + L group, compared with other groups. These results concertedly demonstrated that the incorporation of Dc could potentiate the pro-apoptotic effects of PDT. The synergistic therapy against tumor could be further amplified, largely due to charge reversal-enhanced cellular uptake and ROS-responsive drug release.

In addition to anti-tumor performance, the underlying mechanism behind drug combination were also explored. Firstly, the lactate concentrations in tumor were measured. As shown in Fig. 7E, a lower lactate level was found in Dc&Ce6@MBNP + L group, which can partly explain remarkable tumor suppression relative to other groups. The formulations containing Dc all observed the reduced lactate concentrations in tumor. Then, IF staining results showed Dc&Ce6@MBNP and Dc&Ce6@MBNP + L group had relatively weaker fluorescence intensity, reflective of lower LDHA expression (Fig. 7D). It was consistent with Western blotting analysis (Fig. 7B), where Dc&Ce6@MBNP + L group blocked 40.1% LDHA expression, in contrast with PBS group. Moreover, anti-angiogenesis was evaluated through IHC staining of CD31 antibody, a marker of endothelial cells on blood vessels (Fig. 7F). CD31 expression was high in PBS and Ce6+L group, but significantly reduced in Dc&Ce6@MBNP + L group, similar to 64.9% CD31 suppression shown in Western blotting (Fig. 7C). To delve more deeply into this effect, Western blotting was applied to exploit angiogenesis-related protein expression. Accumulated evidence indicated VEGF-α and angiopoietin-2 (ANGPT2) played essential role in angiogenesis[50], as ANGPT2 is expressed in growing blood vessels and promotes angiogenesis driven by vascular endothelial growth factor (VEGF). Inhibition of both them could bring about complementary and potent anti-angiogenic effects[51,52]. Clearly, a markedly decreased expression of VEGF-α and ANGPT2 was observed in Dc&Ce6@MBNP + L group (Fig. 7A and Supporting Information Fig. S27). The reduction in VEGF-α and anti-angiogenic effects mediated by Dc were also confirmed by other studies[40]. By contrast, enhanced expression of VEGF-α was found in Ce6+L group, consistent with hypoxia-induced resistance to PDT found in other literatures[2,53].

Inspired by Dc-mediated HIF-1α expression inhibition *in vitro*, the expression of HIF-1α in tumor tissues were also evaluated to verify the synergistic effects of Dc. As shown in Fig. 6G, PBS group displayed somewhat hypoxic state in tumor tissue, partly due to the rapid proliferation of tumor cells and deficient oxygen supply from abnormal neovessels. After laser irradiation, Ce6 group showed significantly increased HIF-1α expression, which was explained by Ce6-induced oxygen consumption. The combination of Dc and Ce6 reduced HIF-1α expression, consistent with the results in *in-vitro* HIF-1α expression inhibited by Dc. But relative to free drug combination, Dc&Ce6@MBNP + L decreased slightly but had no significant difference, while Dc&Ce6@BNP + L was a little higher. It also should be pointed out that lactate could mimic hypoxia and stabilize HIF-1α by inhibiting prolyl hydroxylase-2 activity. The oxygen level is not the sole factor determining HIF-1α expression. The subtle difference of HIF-1α expression among three groups could be largely attributed to the delicate balance between the reduction in oxygen that Ce6 caused and HIF-1α and LDHA inhibition of Dc, coupled with different delivery efficiency of nanoparticles[54]. Altogether, these findings strongly supported nanoparticle-delivered Dc sensitized tumors to PDT and overcame the effects of hypoxia in 4T1 mouse model, mainly through the inhibition of neovessels' growth and the reduction of LDHA and HIF-1α expression.

4. Conclusions

In summary, we have proposed a sequentially responsive bilirubin nanocarrier integrated with PDT and LDHA blockade. Morpholine group conferred on this platform an advantage of enhanced cellular uptake in acidic TME. After tumor-specific internalization, a plethora of ROS generation upon laser exposure facilitated the on-demand release of Dc from bilirubin nanoparticles. In this process, PDT caused oxidative damage in tumor sites, but at the same time gave rise to hypoxia, including increased glycolysis and angiogenesis. Meanwhile, the released Dc hampered the activity and expression of LDHA by regulating c-MYC and HIF-1α, accompanied by reduced lactate secretion, to achieve superior anti-angiogenesis, as confirmed by Western blotting analysis and IF staining *in vivo*. This effect added up to a direct strong anti-tumor activity but also sensitized tumor to PDT, by reducing anti-oxidant lactate, to augment the lethality of ROS. As a result, a preferable anti-tumor effect was fulfilled *in vitro* and *vivo*. Although Dc could exert anti-angiogenetic effects through COX-dependent pathway or functional inhibition of MCT, reported by other studies[48], the effect of Dc on LDHA, c-MYC and HIF-1α expression was verified in 4T1 breast cancer cells, which also partly explained its capabilities of anti-glycolysis, anti-angiogenesis and hypoxia pathway modulation. Some differences in the results of other cells, including MCF-7, B16F10 and HUVEC, could reflect the different tumor models used, while Dc might have tumor-specific effects, or the differences in treatment regimens. This strategy would shed lights on the repurposing of diclofenac and LDHA blockade in combating hypoxia-induced

tolerance in many therapeutic modalities, including but not restricted to PDT.

Acknowledgements

The work was supported by National Natural Science Foundation of China (81961138009, China), the Key Research and Development Program of Science and Technology Department of Sichuan Province (No. 2020YFS0570, China), 111 Project (B18035, China) and the Fundamental Research Funds for the Central Universities (China) and the Open Research Fund of Chengdu University of Traditional Chinese Medicine State Key Laboratory of Characteristic Chinese Medicine Resources in Southwest China (China).

Author contributions

Yang Zhou and Huile Gao designed the research. Yang Zhou carried out the experiments and performed data analysis. Fan Tong, Weilong Gu, Siqin He, Xiaotong Yang and Jiamei Li participated part of the experiments. Yang Zhou provided experimental drugs and quality control. Yang Zhou wrote the manuscript. Huile Gao and Yue-Dong Gao revised the manuscript. All of the authors have read and approved the final manuscript.

Conflicts of interest

The authors declare no conflicts of interest.

Appendix A. Supporting information

Supporting data to this article can be found online at https://doi.org/10.1016/j.apsb.2021.12.001.

References

1. Fan WP, Huang P, Chen XY. Overcoming the Achilles' heel of photodynamic therapy. *Chem Soc Rev* 2016;**45**:6488−519.
2. Xie JL, Wang YW, Choi WS, Jangili P, Ge YQ, Xu YJ, et al. Overcoming barriers in photodynamic therapy harnessing nano-formulation strategies. *Chem Soc Rev* 2021;**50**:9152−201.
3. Schito L, Semenza GL. Hypoxia-inducible factors: master regulators of cancer progression. *Trends Cancer* 2016;**2**:758−70.
4. Denko NC. Hypoxia, HIF1 and glucose metabolism in the solid tumour. *Nat Rev Cancer* 2008;**8**:705−13.
5. Nakazawa MS, Keith B, Simon MC. Oxygen availability and metabolic adaptations. *Nat Rev Cancer* 2016;**16**:663−73.
6. Sonveaux P, Copetti T, De Saedeleer CJ, Vegran F, Verrax J, Kennedy KM, et al. Targeting the lactate transporter MCT1 in endothelial cells inhibits lactate-induced HIF-1 activation and tumor angiogenesis. *PLoS One* 2012;**7**:e33418.
7. De Saedeleer CJ, Copetti T, Porporato PE, Verrax J, Feron O, Sonveaux P. Lactate activates HIF-1 in oxidative but not in Warburg-phenotype human tumor cells. *PLoS One* 2012;**7**:e46571.
8. Brown TP, Ganapathy V. Lactate/GPR81 signaling and proton motive force in cancer: role in angiogenesis, immune escape, nutrition, and Warburg phenomenon. *Pharmacol Ther* 2020;**206**:107451.
9. Vegran F, Boidot R, Michiels C, Sonveaux P, Feron O. Lactate influx through the endothelial cell monocarboxylate transporter MCT1 supports an NF-κB/IL-8 pathway that drives tumor angiogenesis. *Cancer Res* 2011;**71**:2550−60.
10. Lee DC, Sohn HA, Park ZY, Oh SH, Kang YK, Lee KM, et al. A lactate-induced response to hypoxia. *Cell* 2015;**161**:595−609.
11. Ippolito L, Morandi A, Giannoni E, Chiarugi P. Lactate: a metabolic driver in the tumour landscape. *Trends Biochem Sci* 2019;**44**:153−66.
12. Feng YB, Xiong YL, Qiao TY, Li XF, Jia LT, Han Y. Lactate dehydrogenase A: a key player in carcinogenesis and potential target in cancer therapy. *Cancer Med* 2018;**7**:6124−36.
13. Shim H, Dolde C, Lewis BC, Wu CS, Dang G, Jungmann RA, et al. C-Myc transactivation of LDH-A: implications for tumor metabolism and growth. *Proc Natl Acad Sci USA* 1997;**94**:6658−63.
14. Dang CV, Le A, Gao P. MYC-induced cancer cell energy metabolism and therapeutic opportunities. *Clin Cancer Res* 2009;**15**:6479−83.
15. Le A, Cooper CR, Gouw AM, Dinavahi R, Maitra A, Deck LM, et al. Inhibition of lactate dehydrogenase A induces oxidative stress and inhibits tumor progression. *Proc Natl Acad Sci USA* 2010;**107**:2037−42.
16. Fantin VR, St-Pierre J, Leder P. Attenuation of LDH-A expression uncovers a link between glycolysis, mitochondrial physiology, and tumor maintenance. *Cancer Cell* 2006;**9**:425−34.
17. Serganova I, Cohen IJ, Vemuri K, Shindo M, Maeda M, Mane M, et al. LDH-A regulates the tumor microenvironment *via* HIF-signaling and modulates the immune response. *PLoS One* 2018;**13**:e203965.
18. Gottfried E, Lang SA, Renner K, Bosserhoff A, Gronwald W, Rehli M, et al. New aspects of an old drug—diclofenac targets MYC and glucose metabolism in tumor cells. *PLoS One* 2013;**8**:e66987.
19. Chirasani SR, Leukel P, Gottfried E, Hochrein J, Stadler K, Neumann B, et al. Diclofenac inhibits lactate formation and efficiently counteracts local immune suppression in a murine glioma model. *Int J Cancer* 2013;**132**:843−53.
20. Leidgens V, Seliger C, Jachnik B, Welz T, Leukel P, Vollmann-Zwerenz A, et al. Ibuprofen and diclofenac restrict migration and proliferation of human glioma cells by distinct molecular mechanisms. *PLoS One* 2015;**10**:e140613.
21. Pandey SK, Yadav S, Goel Y, Temre MK, Singh VK, Singh SM. Molecular docking of anti-inflammatory drug diclofenac with metabolic targets: potential applications in cancer therapeutics. *J Theor Biol* 2019;**465**:117−25.
22. Hu C, He XQ, Chen YX, Yang XT, Qin L, Lei T, et al. Metformin mediated PD-L1 downregulation in combination with photodynamic-immunotherapy for treatment of breast cancer. *Adv Funct Mater* 2021;**31**:2007149.
23. Allison RR. Photodynamic therapy: oncologic horizons. *Future Oncol* 2014;**10**:123−4.
24. Zhao LZ, Li JY, Su YQ, Yang LQ, Chen L, Qiang L, et al. MTH1 inhibitor amplifies the lethality of reactive oxygen species to tumor in photodynamic therapy. *Sci Adv* 2020;**6**:z575.
25. Wiktorowska-Owczarek A. The effect of diclofenac on proliferation and production of growth factors by endothelial cells (HMEC-1) under hypoxia and inflammatory conditions. *Acta Pharm* 2014;**64**:131−8.
26. Boelsterli U. Diclofenac-induced liver injury: a paradigm of idiosyncratic drug toxicity. *Toxicol Appl Pharmacol* 2003;**192**:307−22.
27. Vyas A, Purohit A, Ram H. Assessment of dose-dependent reproductive toxicity of diclofenac sodium in male rats. *Drug Chem Toxicol* 2019;**42**:478−86.
28. Sun QH, Zhou ZX, Qiu NS, Shen YQ. Rational design of cancer nanomedicine: nanoproperty integration and synchronization. *Adv Mater* 2017;**29**:1606628.
29. Zhang W, Wang F, Hu C, Zhou Y, Gao HL, Hu J. The progress and perspective of nanoparticle-enabled tumor metastasis treatment. *Acta Pharm Sin B* 2020;**10**:2037−53.
30. Hu J, Yuan XW, Wang F, Gao HL, Liu XL, Zhang W. The progress and perspective of strategies to improve tumor penetration of nanomedicines. *Chin Chem Lett* 2021;**32**:1341−7.
31. Lee YH, Lee SY, Lee DY, Yu BJ, Miao WJ, Jon SY. Multistimuli-responsive bilirubin nanoparticles for anticancer therapy. *Angew Chem Int Ed Engl* 2016;**55**:10676−80.
32. Lee YH, Sugihara K, Gillilland MG, Jon SY, Kamada N, Moon JJ. Hyaluronic acid-bilirubin nanomedicine for targeted modulation of

dysregulated intestinal barrier, microbiome and immune responses in colitis. *Nat Mater* 2020;**19**:118−26.
33. Palayoor ST, Tofilon PJ, Coleman CN. Ibuprofen-mediated reduction of hypoxia-inducible factors HIF-1alpha and HIF-2alpha in prostate cancer cells. *Clin Cancer Res* 2003;**9**:3150−7.
34. Ordway B, Tomaszewski M, Byrne S, Abrahams D, Swietach P, Gillies RJ, et al. Targeting of evolutionarily acquired cancer cell phenotype by exploiting pHi-metabolic vulnerabilities. *Cancers* 2021; **13**:64.
35. Zhang Y, Wang CH, Xu C, Yang CP, Zhang ZQ, Yan HS, et al. Morpholino-decorated long circulating polymeric micelles with the function of surface charge transition triggered by pH changes. *Chem Commun* 2013;**49**:7286.
36. Chen JJ, Ding JX, Xu WG, Sun TM, Xiao HH, Zhuang XL, et al. Receptor and microenvironment dual-recognizable nanogel for targeted chemotherapy of highly metastatic malignancy. *Nano Lett* 2017; **17**:4526−33.
37. Hu C, Lei T, Wang YS, Cao J, Yang XT, Qin L, et al. Phagocyte-membrane-coated and laser-responsive nanoparticles control primary and metastatic cancer by inducing anti-tumor immunity. *Biomaterials* 2020;**255**:120159.
38. Liu R, Yu ML, Yang XT, Umeshappa CS, Hu C, Yu WQ, et al. Linear chimeric triblock molecules self-assembled micelles with controllably transformable property to enhance tumor retention for chemo-photodynamic therapy of breast Cancer. *Adv Funct Mater* 2019;**29**: 1808462.
39. Lin CC, Tong F, Liu R, Xie R, Lei T, Chen YX, et al. GSH-responsive SN38 dimer-loaded shape-transformable nanoparticles with iRGD for enhancing chemo-photodynamic therapy. *Acta Pharm Sin B* 2020;**10**: 2348−61.
40. Mayorek N, Naftali-Shani N, Grunewald M. Diclofenac inhibits tumor growth in a murine model of pancreatic cancer by modulation of VEGF levels and arginase activity. *PLoS One* 2010;**5**:e12715.
41. Yang XT, Hu C, Tong F, Liu R, Zhou Y, Qin L, et al. Tumor microenvironment-responsive dual drug dimer-loaded PEGylated bilirubin nanoparticles for improved drug delivery and enhanced immunechemotherapy of breast cancer. *Adv Funct Mater* 2019;**29**:1901896.
42. Zhang RY, Xing RR, Jiao TF, Ma K, Chen CJ, Ma GH, et al. Carrier-free, chemophotodynamic dual nanodrugs *via* self-assembly for synergistic antitumor therapy. *ACS Appl Mater Interfaces* 2016;**8**:13262−9.
43. Liang K, Chung JE, Gao SJ, Yongvongsoontorn N, Kurisawa M. Highly augmented drug loading and stability of micellar nanocomplexes composed of doxorubicin and poly(ethylene glycol)-green tea catechin conjugate for cancer therapy. *Adv Mater* 2018;**30**:1706963.
44. Yongvongsoontorn N, Chung JE, Gao SJ, Bae KH, Yamashita A, Tan MH, et al. Carrier-enhanced anticancer efficacy of sunitinib-loaded green tea-based micellar nanocomplex beyond tumor-targeted delivery. *ACS Nano* 2019;**13**:7591−602.
45. Chung JE, Tan SS, Gao SJ, Yongvongsoontorn N, Kim SH, Lee JH, et al. Self-assembled micellar nanocomplexes comprising green tea catechin derivatives and protein drugs for cancer therapy. *Nat Nanotechnol* 2014;**9**:907−12.
46. Li YP, Sun XX, Qian DZ, Dai MS. Molecular crosstalk between MYC and HIF in cancer. *Front Cell Dev Biol* 2020;**8**:590576.
47. Serganova I, Rizwan A, Ni XH, Thakur SB, Vider J, Russell J, et al. Metabolic imaging: a link between lactate dehydrogenase A, lactate, and tumor phenotype. *Clin Cancer Res* 2011;**17**:6250−61.
48. Renner K, Bruss C, Schnell A, Koehl G, Becker HM, Fante M, et al. Restricting glycolysis preserves T cell effector functions and augments checkpoint therapy. *Cell Rep* 2019;**29**:135−50.
49. Jain M, Arvanitis C, Chu K, Dewey W, Leonhardt E, Trinh M, et al. Sustained loss of a neoplastic phenotype by brief inactivation of MYC. *Science* 2002;**297**:102−4.
50. Huang HH, Bhat A, Woodnutt G, Lappe R. Targeting the ANGPT-TIE2 pathway in malignancy. *Nat Rev Cancer* 2010;**10**: 575−85.
51. Hashizume H, Falcón BL, Kuroda T, Baluk P, Coxon A, Yu D, et al. Complementary actions of inhibitors of angiopoietin-2 and VEGF on tumor angiogenesis and growth. *Cancer Res* 2010;**70**: 2213−23.
52. Schmittnaegel M, Rigamonti N, Kadioglu E, Cassara A, Wyser RC, Kiialainen A, et al. Dual angiopoietin-2 and VEGFA inhibition elicits antitumor immunity that is enhanced by PD-1 checkpoint blockade. *Sci Transl Med* 2017;**9**:eaak9670.
53. Lecaros RL, Huang L, Lee TC, Hsu YC. Nanoparticle delivered VEGF-A siRNA enhances photodynamic therapy for head and neck cancer treatment. *Mol Ther* 2016;**24**:106−16.
54. Rey S, Schito L, Wouters BG, Eliasof S, Kerbel RS. Targeting hypoxia-inducible factors for antiangiogenic cancer therapy. *Trends Cancer* 2017;**3**:529−41.